SPACE ROBOTS

A 2-year locomotive exploration and scientific investigation of the lunar farside by the Yutu-2 rover

L. Ding[1]*†, R. Zhou[1]†, Y. Yuan[1]†, H. Yang[1], J. Li[2], T. Yu[2]*, C. Liu[2,3], J. Wang[2], S. Li[1], H. Gao[1]*, Z. Deng[1], N. Li[1], Z. Wang[1], Z. Gong[1], G. Liu[4], J. Xie[2], S. Wang[2], Z. Rong[2], D. Deng[2], X. Wang[2,3], S. Han[2], W. Wan[5], L. Richter[6], L. Huang[1], S. Gou[5], Z. Liu[1], H. Yu[1], Y. Jia[7], B. Chen[7], Z. Dang[7], K. Zhang[2], L. Li[2], X. He[2], S. Liu[2], K. Di[5]

The lunar nearside has been investigated by many uncrewed and crewed missions, but the farside of the Moon remains poorly known. Lunar farside exploration is challenging because maneuvering rovers with efficient locomotion in harsh extraterrestrial environment is necessary to explore geological characteristics of scientific interest. Chang'E-4 mission successfully targeted the Moon's farside and deployed a teleoperated rover (Yutu-2) to explore inside the Von Kármán crater, conveying rich information regarding regolith, craters, and rocks. Here, we report mobile exploration on the lunar farside with Yutu-2 over the initial 2 years. During its journey, Yutu-2 has experienced varying degrees of mild slip and skid, indicating that the terrain is relatively flat at large scales but scattered with local gentle slopes. Cloddy soil sticking on its wheels implies a greater cohesion of the lunar soil than encountered at other lunar landing sites. Further identification results indicate that the regolith resembles dry sand and sandy loam on Earth in bearing properties, demonstrating greater bearing strength than that identified during the Apollo missions. In sharp contrast to the sparsity of rocks along the traverse route, small fresh craters with unilateral moldable ejecta are abundant, and some of them contain high-reflectance materials at the bottom, suggestive of secondary impact events. These findings hint at notable differences in the surface geology between the lunar farside and nearside. Experience gained with Yutu-2 improves the understanding of the farside of the Moon, which, in return, may lead to locomotion with improved efficiency and larger range.

INTRODUCTION

Planetary exploration using orbiters or rovers has continued to extend the boundaries of science and technology in the last few decades (*1*–*3*). The Moon, the closest celestial body to Earth with potentially exploitable chemical and mineralogical resources (*4*), is one of the most substantial destinations of exploration missions. The lunar exploration effort peaked after the successful Apollo program; since then, there have been 20 successful landers on the near side of the Moon as a result of crewed and rover-based missions. However, no astronauts or landers arrived on the lunar farside until 2019, mainly due to the blindness of the side with respect to communication and monitoring, although evidence collected through remote sensing had indicated the distinction of the two sides in gravitational field (*5*) and material composition (*6*), providing a strong impetus for in situ exploration of the farside. The Chang'E-4 (CE-4) lunar exploration mission with the Yutu-2 rover was the first mission attempting to land on the farside of the Moon and was expected to make valuable and important scientific discoveries through in situ exploration.

Since the successful landing of the CE-4 probe (fig. S1A) on 3 January 2019, at 177.6°E, 45.4°S on the lunar farside in the Von Kármán crater inside the South Pole–Aitken (SPA) basin, Yutu-2 has been continuing scientific exploration for more than two Earth years (25 lunar days) (*7*). Yutu-2, as the lightest-ever lunar rover (135 kg), is a six-wheeled high-performance off-road robot equipped with four steering motors at the corner wheels, having a maximum speed capability of 200 m/hour (about 0.056 m/s). Benefiting from the well-designed rocker-bogie structure, Yutu-2 can climb up 20° slopes and surmount obstacles up to 200-mm high (*8*). The meshed surface of the wheels makes them light (735 g; diameter of 300 mm and width of 150 mm) (fig. S1B), and the lugs attached to the wheels enhance the rover's driving performance. Yutu-2 carries four scientific payloads (fig. S1C) to acquire high-resolution images and high-accuracy data, including a panoramic camera (Pancam), a visible and near-infrared image spectrometer (VNIS), a lunar penetrating radar (LPR) (*9*), and an Advanced Small Analyzer for Neutrals (ASAN) (*10*). Its high-reliability locomotion system enabled Yutu-2 to survive beyond the designed 3-month life span, expanding its exploration distance to 600.55 m at the end of the first 2 years, leading to richer scientific insights from the unexplored zone. Over the course of the first 2 years, about 16.46 gigabytes of scientific data have been return-transmitted and analyzed, thus filling the gaps of geological knowledge of the lunar farside and deepening the understanding of the Moon's formation and evolution.

Here, we present locomotive data and images collected by Yutu-2 rover that reveal unique characteristics of the lunar farside. In addition, results of wheel slippage and sinkage, along with an analysis of the lunar regolith properties using the wheel-terrain interaction model, are presented. A comprehensive review of the scientific investigations carried out by Yutu-2 in craters, rocks, and stratum was carried out with additional analyses. On the basis of the discovered distinct geological features on the lunar farside, more powerful rovers, as well as scientific payloads and theoretical conundrums

[1]State Key Laboratory of Robotics and System, Harbin Institute of Technology, Harbin 150080, China. [2]Beijing Aerospace Control Center, Beijing 100094, China. [3]Key Laboratory of Science and Technology on Aerospace Flight Dynamics, Beijing 100094, China. [4]Department of Aerospace Engineering, Ryerson University, Toronto, ON M5B 2K3, Canada. [5]State Key Laboratory of Remote Sensing Science, Aerospace Information Research Institute, Chinese Academy of Sciences, Beijing 100101, China. [6]Large Space Structures GmbH, Hauptstrasse 1, D-85386 Eching, Germany. [7]China Academy of Space Technology, Beijing 100094, China.
*Corresponding author. Email: liangding@hit.edu.cn (L.D.); yuty.bacc@foxmail.com (T.Y.); gaohaibo@hit.edu.cn (H.G.)
†These authors contributed equally to this work.

on complex wheel-terrain interaction mechanisms, are exposed and realized to be necessary for future robotic lunar explorations.

RESULTS

Travel route and wheel slippage

The Queqiao relay satellite (*11*), which is the first relay communication satellite outside Earth's orbit and features the largest satellite umbrella antenna diameter (4.2 m), acts as a high-speed bridge to transmit data and commands between the ground station and Yutu-2, with a time delay of 1 to 2 s in one-way transmission. Yutu-2 has navigated toward the northwest (Fig. 1A) using a three-layered planning architecture, in which three-dimensional (3D) lunar surface data with 7-m resolution obtained from the CE-2 mission were used for long-term planning; the panoramic images were analyzed to generate roving trajectories for each lunar day, whereas the navigation images were used for replanning. Primarily, Yutu-2 was directly controlled by uploaded commands generated from ground teleoperation; however, it can also work in autonomous mode on relatively flat terrains, planning traversable routes using its laser lattice or hazard avoidance camera (Hazcam). The autonomous mode of Yutu-2 was used in a traverse of 2.7 m on the fifth lunar day, in which autonomous planning was carried out five times, and each planning segment was about 0.5 m. A vision-based decision-supporting method (*12*) consisting of obstacle map generation and path evaluation was used to ensure Yutu-2's efficiency and safety. The physical properties of surface regolith strongly affected Yutu-2's traverse trajectories, wheel slippages, and sinkage, which was, in turn, used to infer terrain properties in the tangential and normal directions.

The wheel slip ratios (hereafter referred to as slip ratios) for each lunar day (calculated using planned and actual travel distances derived from visual measurements between adjacent waypoints) (Fig. 1B) indicate that Yutu-2 experienced relatively small wheel slipping and skidding. The slip ratios (defined as a function of the theoretical circumference velocity and the actual traveling longitudinal velocity of the wheel) ranged from −0.15 to 0.15 and, in most cases, were within the range of 0 to 0.05, consistent with the observed small elevation variations along the traversed routes (fig. S2). On the ninth lunar day, the rover struggled to explore a localized fresh crater with shiny materials through several short approaching attempts without accurate visual localization on waypoints. Therefore, it was not possible to calculate the corresponding average slip ratios between any two adjacent waypoints, and they are missing from Fig. 1B. However, wheel trace imprints left by Yutu-2 gave clues to the wheel slip ratios experienced during the complex movements (a to b, b to a, a to c, c to d, and d to c) as shown in Fig. 2. Fine-grained slip ratios based on clear and intact trace imprints (red frames in Fig. 2) were estimated using the slip ratio estimation model (*13*) by extracting the trace units as shown in fig. S3. When retracting from the crater (b to a and d to c), the estimated slip ratio was about −0.1, which was consistent with the decreased slope (3.10°) when departing from the crater rim. According to the symmetry mechanism of the slip ratio in the elastic phase ($-0.1 < s < 0.1$) (*14*), the slip ratio when maneuvering up the slope (a to b and c to d) was estimated as 0.1. The calculated slippage result (b to a; $s \approx -0.1$) was close to that when backing out from the other side of the crater (d to c; $s \approx -0.1$) but larger than that when roving on the flat surface (a to c; $s \approx 0.0$), hinting that the stack ejecta was similar in terms of slope and properties on these two sides of the crater. Slip ratios derived

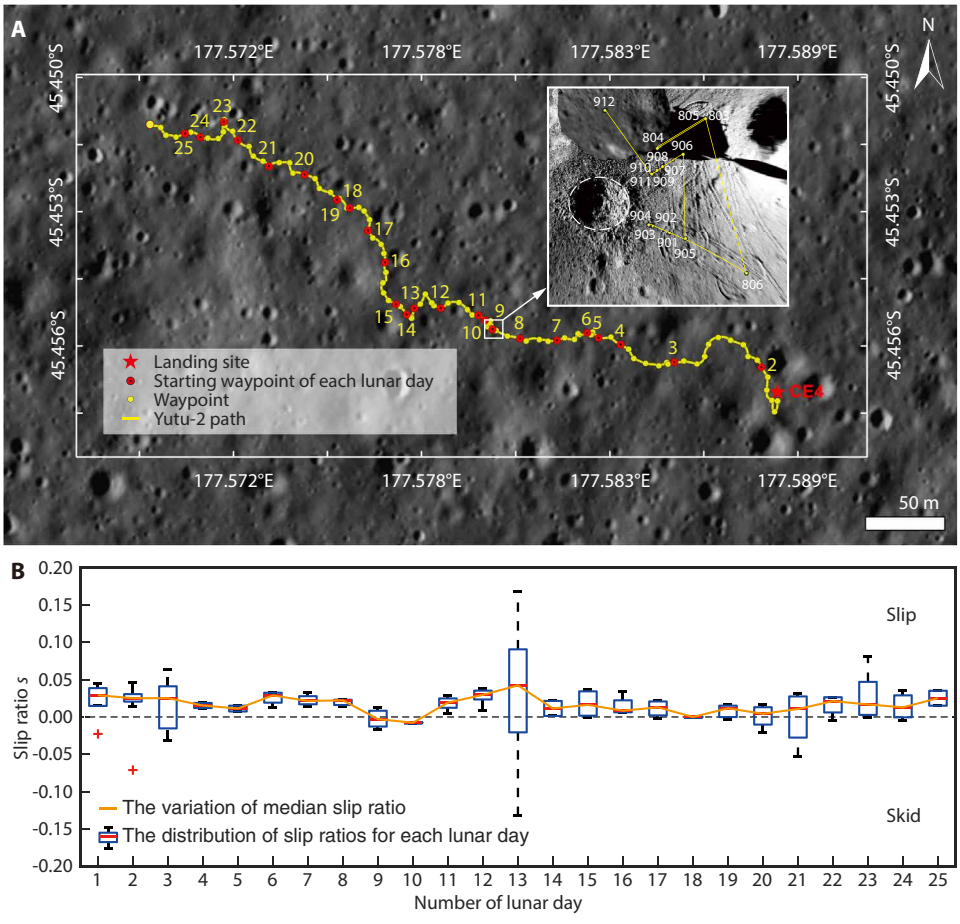

Fig. 1. Yutu-2's routing path and slippage on the farside of the Moon. (**A**) Routing path of the rover. The yellow dots represent waypoints. The red dots represent Yutu-2's starting waypoint of each lunar day; they are also the sleeping waypoint of the last lunar day. The rover passed through 132 waypoints in the first 25 lunar days. The exploration phase of the eighth and ninth lunar day is zoomed in to show detailed traverse routes. The base image is a high-resolution (0.9 m per pixel) digital orthophoto map (DOM) (*60*) generated from LROC narrow angle camera (NAC) imagery (*61*). (**B**) Box plot of Yutu-2's wheel slip ratios along the routing path on each lunar day. Paths that are too short were dismissed in the statistics because they were usually without visual localization results or introduced too many errors. Paths controlled in driving time without planned target waypoints were also dismissed.

from wheel trace imprints over short traverses helped to characterize the wheel slip experienced in local terrain, complementing the average slip ratios between two adjacent waypoints as shown in Fig. 1B.

Soil physical properties

After a 1.96-m traverse from waypoints LE00804 to LE00805 (while backing from the crater), large agglomerates of cloddy soil were observed adhering onto Yutu-2's wheels (Fig. 3A). This can be compared with a previous CE-3 mission during which the earlier Yutu rover experienced a similar traverse at the mission site of Mare Imbrium; only sticky and fine particles were observed on the wheels (Fig. 3B). Although the wheels of Yutu were in the same configuration as that of Yutu-2, the soil adhesion was negligible. According to the region division results (fig. S4), more than 46% of the wheel surface shown in the subfigure of Fig. 3A was covered with the cloddy soil, which is much larger than the coverage ratio observed on the wheels of CE-3 Yutu (~2%; calculated using the subfigure of Fig. 3B). Similar sharp contrasts between the Yutu-2 and Yutu rovers, with respect to soil sticking to wheels, are also presented on their mutual shooting images (fig. S5). The sticky fine particles on Yutu's wheels during CE-3 were most likely due to electrostatic adhesion, but the larger pieces of soil on Yutu-2's wheels during CE-4 are unusual. Furthermore, Yutu-2 observed similar phenomena on other lunar days, as portrayed by wheel images taken throughout the 4th, 5th, 6th, 19th, and 23rd lunar days of the entire 600.55-m journey (fig. S6). Thus, it is reasonable to assume that, at the CE-4 landing site, the greater cohesion of the soil is regional rather than localized. The increased cohesion of the lunar regolith on the CE-4 landing site is likely attributed to the higher percentage of agglutinates in the lunar regolith, which is in proportion with the soil maturity. This is supported by the findings that the Is/FeO maturity index of the CE-4 landing site (82 ± 15) (*15*) is higher than that of the CE-3 landing site (~53) (*16*), which indicates that the lunar soil at the CE-4 landing site is more mature than that at the CE-3 landing site (*17*). According to the theory of plastic equilibrium, cohesion of materials is the bond that cements particles together, irrespective of the normal pressure exerted by one particle upon the others. On the other hand, particles of frictional masses can be held together only when a normal pressure exists among them (*18*). With agglutinates, soil particles are more likely to agglomerate (hold together or build bond) when ground by the wheel, which changes the loose structure of aeolian sand soil, resulting in an increase in the solidification cohesion of the soil. Such blocky soil on the wheels would weaken the digging effect of the wheel lugs and consequently reduce the drawbar pull, which would be unfavorable to the rover's traction. Because most soil was observed to adhere on the wheel lugs rather than the high-porosity meshed surface, this situation may be improved in future missions by coating the lugs' surface with a special anti-adhesion material.

Although Yutu-2 does not carry specific soil parameter identification instruments, the rover wheel can be used as a trenching device to identify soil parameters based on the wheel-terrain interaction. Regarding regolith properties, the normal bearing characteristics of the regolith around the landing site can be inferred based on wheel sinkage. During Yutu-2's drive to point A (fig. S7) for mutual shooting, its wheels were almost supported only by lugs (the wheel rim was visibly in contact with the ground), but it sometimes sank slightly into the terrain and experienced moderate soil seepage into the wire mesh

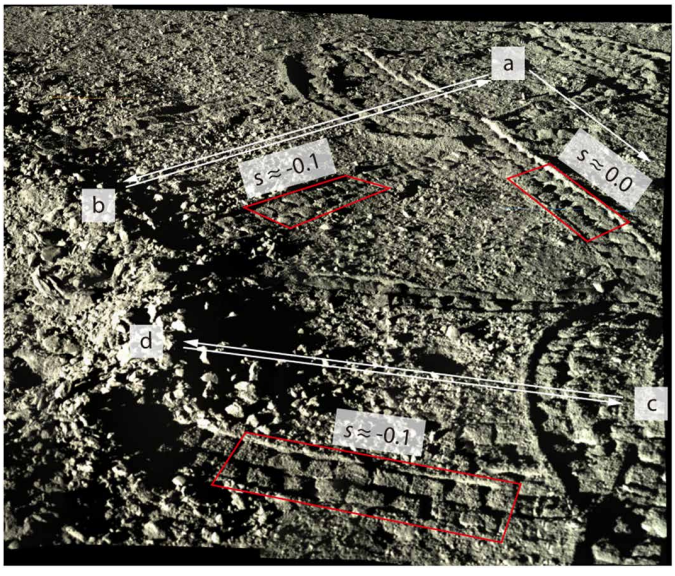

Fig. 2. Yutu-2's wheel imprints and reflected slippage. Yutu-2 first drove toward the target crater along trajectory a→b but failed in acquiring adequate data. Thus, it planned to approach the crater again from the northwest of the crater along the route c→d after coming down from the crater and turning around in circles to adjust direction. The wheel slip ratios estimated based on fragments of clear and intact trace imprints outlined by the red lines during the traverse of b→a, a→c, and d→c were estimated approximately as −0.1, 0, and −0.1, respectively. The image was taken by Pancam at the ninth lunar day at waypoint LE00912.

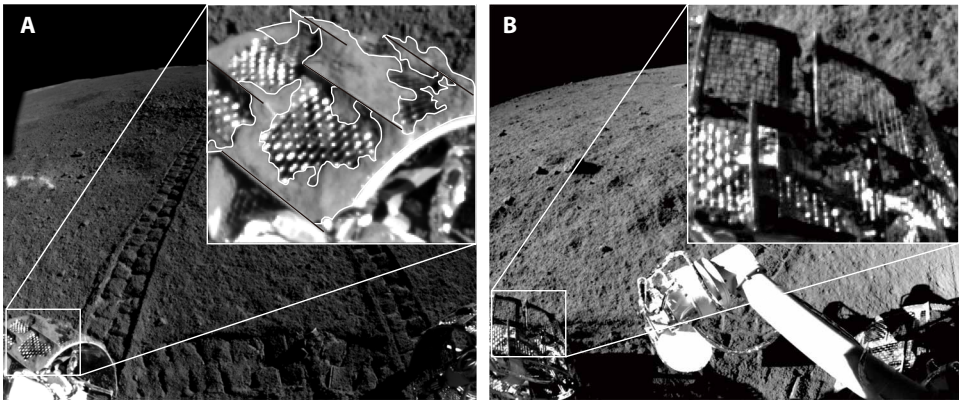

Fig. 3. Soil sticky phenomenon of Yutu-2 compared with Yutu. (**A**) Large pieces of irregular-shaped lunar soil sticking to Yutu-2's front left wheel. The image was taken by Hazcam of Yutu-2 on the ninth lunar day on CE-4 mission. (**B**) No soil adhesion on Yutu's front left wheel, which is clean with only fine particles. The image was taken by Hazcam after Yutu's arm dropped on CE-3 mission.

screen. By correcting the view to the orthographic angle of the wheel side images and calculating the proportion of the wheel sinkage to the wheel radius in the image (see Materials and Methods), the equivalent wheel sinkage was estimated to be 5 to 15 mm. Compared with the wheel sinkage estimated at the CE-3 landing site (5.6 to 11.5 mm) (*18*), its range in CE-4 (5 to 15 mm) is a bit larger, under almost the same wheel load (22.5 kg per wheel). The wheel sinkage of Lunokhod 1 in the Luna 17 mission was much larger (10.7 to 25.4 mm) (*19*) under a heavier load (94.5 kg per wheel). According to the terramechanics model for lugged wheels (*20*) (Fig. 4A) and wheel-terrain interaction parameters (table S1), we predicted the curves reflecting the regolith bearing property parameters under different sinkage conditions (Fig. 4B). Comparatively, the region of the estimated bearing parameters at CE-3 (the region within two purple curves, Fig. 4A) mostly overlaps with that of the Luna 17 landing site (the region between two orange curves, Fig. 4A), whereas it has a larger equivalent sinkage modulus under the same sinkage exponent than that of CE-4 on average. This indicates that the lunar regolith at the CE-3 and Luna 17 sites is relatively stronger in bearing strength than that at the CE-4 site. Assuming that the equivalent stiffness was 820 kPa/m^N (*21*) (close to the typical value of the friction deformable modulus for lunar soil derived from Apollo missions; shown as the gray dashed line in Fig. 4B), the sinkage exponent (denoted by N) ranged from 0.83 to 1.0. When the sinkage exponent was assumed to be 1.0 (*22*) (the typical value of lunar soil deduced from Apollo missions), the corresponding equivalent stiffness was 840 to 2800 kPa/m^N. When the sinkage exponent and the equivalent stiffness modulus (denoted by K_s) were both assumed to be above the typical values of lunar regolith, the wheel sinkage (the intersection of the two gray dashed lines) was about 15.5 mm, larger than the average wheel sinkage observed, implying that the regolith at the landing site is stronger than the typical lunar soil of Apollo missions. As demonstrated in Fig. 4C, the bearing property of the regolith at the landing site on the lunar farside is analogous to that of dry sand and sandy loam (table S2) on Earth (*18*).

Scientific investigations in terms of craters, rocks, and stratum

Benefiting from Yutu-2's locomotive venture consisting of a series of careful movements during the first 25 lunar days, in situ investigations of lunar rocks (*22*–*24*), soil (*25*–*30*), impact craters (*28*, *31*–*33*), and energetic neutral atoms emitted from the lunar surface (*34*) have been carried out on the farside of the Moon, as summarized chronologically in Table 1. Taking advantage of Yutu-2's scientific payloads (Pancam, VNIS, LPR, and ASAN), most of the primary scientific objectives (*35*) of the CE-4 mission have been accomplished, including (i) low-frequency astronomical study on the lunar surface, (ii) shallow structural investigation of the roving area on the lunar farside, and (iii) topographic and mineralogical composition investigation of the roving area on the lunar farside. These results have established a foundation for subsequent in-depth studies. During this 2-year venture, one of the most exciting explorations involved the rover taking a risk of instability at the rim of a 2-m crater on the eighth lunar day, owing to the detection of an unexpected gel-like material of high reflectance discovered at the crater's base. The dark greenish, glistening material (Fig. 5A) viewed by Pancam at the closest safe distance from the crater after two painstaking approach-attempts showed its distinctive shape, color, and texture from the surrounding regolith blocks (*28*). The material's appearance, which resembles lunar samples 15466 and 70019 obtained by the Apollo 15 and 17 missions, suggests that it could be an impact melt breccia or a glass-coated agglutinitic regolith breccia with a possible complex formation of impact-generated welding, cementing, and agglutination of lunar regolith and breccia (*28*).

An inspection of the gel-like material, and even entering the crater, to conduct close-focused investigation using payloads would be of great scientific interest. However, because of the high probability of locomotor failures, the rover has been advised to limit any further movement. If Yutu-2 drove down along the steep crater wall, it might be out of control due to the skid failure of the wheels. Furthermore, even if it enters the crater successfully, the rover will find maneuvering out of the crater highly difficult, according to

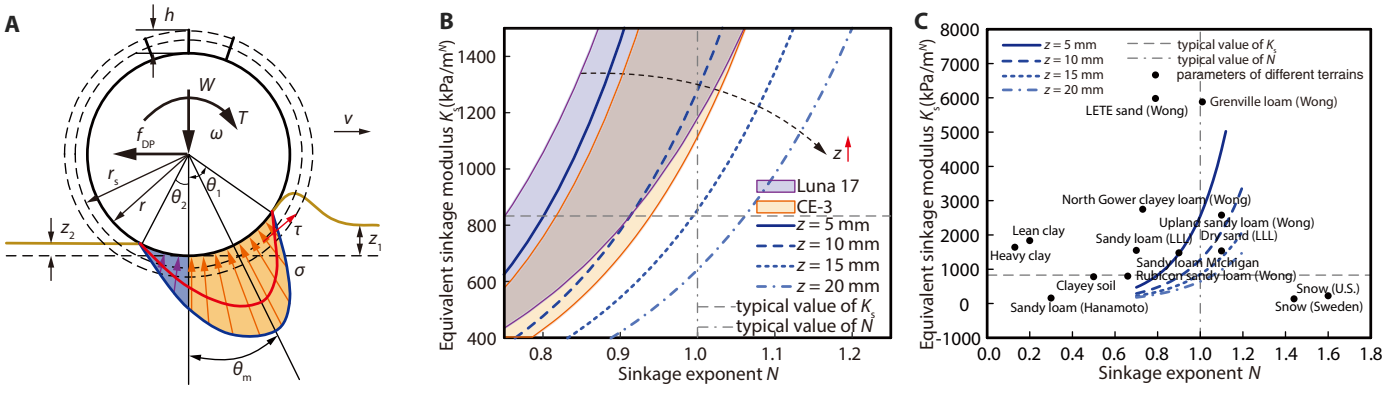

Fig. 4. Soil parameter identification. (**A**) Force diagram of wheel-terrain interaction of a planetary rover (*20*). The blue area is of active earth pressure, and the yellow area is of passive earth pressure. The blue curve circled area is where the normal stress occurred, whereas the red curve circled area is where the shear stress occurred. (**B**) Bearing characteristic curve under different wheel sinkage conditions. The blue region within the two purple lines corresponds to the bearing parameters under Lunokhod 1's wheel sinkage range in Luna 17 mission. The yellow region between the two orange lines corresponds to the bearing parameters under Yutu's wheel sinkage range in CE-3 mission. (**C**) Bearing characteristic curve with bearing parameters of terrains on Earth. The bearing parameters of terrains on Earth are listed in table S2. In (B) and (C), N is the variable sinkage exponent of wheel-terrain interaction; for black scatter points representing parameters of terrains on Earth and the dashed-dotted lines representing typical parameters of terrains on the Moon, $N = n$ (intrinsic sinkage exponent of the terrain).

Table 1. Daily scientific exploration and key findings. The total working time of Yutu-2 was about 4019 hours for the first 25 lunar days. On most lunar days, Yutu-2 carried out routine navigation and detection using VNIS and LPR. It switched to rest mode at lunar night and noon due to the extreme temperatures. Key findings based on data collected on each lunar day are listed, beginning with asterisks and corresponding payloads, whereas special scientific exploration activities are listed without asterisks. LDay is an abbreviation for lunar day.

Lunar day number	Accumulated distance (m)	Scientific exploration and key findings
1	44.19	*VNIS: Mental-derived materials in low-calcium pyroxene and olivine (*30*)
		Two-way mutual shooting
2	120.01	*LPR (LDay 1 and 2): The first high-resolution image of a lunar ejecta sequence and its thickness as well as internal architecture (*41*)
3	162.99	*LPR: Lunar regolith source and a three-unit substructure at the landing site (*25*)
		*VNIS and Pancam: An olivine-norite rock likely crystallized from the SPA-impact melt pool rich in plagioclase probably ejected from the Zhinyu crater (*22*)
4	178.97	Routine navigation and detection
5	190.77	*LPR: Dielectric properties and structure of lunar regolith (*27*)
		Detection of the first solar energetic particle (SEP) event with Lunar Lander Neutron and Dosimetry on the CE-4 lander (*34*)
6	213.04	Imaging of wheel trace with Pancam
7	237.92	The farthest distance of a single walk (9.02 m) on the lunar farside
		Neutral atom detection facing the sun and facing away from the sun for 4 hours, respectively, with ASAN
8	271.03	*Pancam: Discovery of high-reflection materials
9	284.66	*VNIS and Pancam: A dark greenish and glistening impact melt breccia in a crater and surrounding regolith in mixture of multiple sources (*28*)
		*LPR: The same physical properties between the beneath blocky ejecta deposits and the surrounding regolith, and observed fragments not originated from the subsurface (*32*)
		*LPR (LDay 1 to 9): Deep subsurface structure of at least four layers of distinct lava flows and their thickness (*43*)
10	289.77	*VNIS: Ground-truth Hapke parameters provided for remote sensing observation (*63*)
11	318.62	Multipoint detection
12	345.06	*LPR: The shallow regolith structure and deep geological strata below the landing site (*42*)
13	357.70	Neutral atom detection for solar wind energy spectrum distribution
14	367.25	Neutral atom detection facing the sun and facing away from the sun for 4 hours, respectively, with ASAN
15	399.79	Detection of impact ejecta in front of a crater, and panoramic color imaging of the impact crater and mysterious substances in its center
16	424.45	Routine navigation and detection
17	447.68	*Pancam: Discovery of a crater with gel-like material
18	447.68	Due to the plan of launch Tianwen-1, scientific payloads of Yutu-2 stay switch off
19	463.26	Detection of a crater found on the 17th lunar day with VNIS and its ejecta on the west side of the crater
20	490.90	Routine navigation and detection
21	519.29	Routine navigation and detection
22	547.18	Routine navigation and detection
23	565.90	Panoramic color imaging of a large impact crater named Longtan, detection of small rocks on the southwest side of the impact crater, and updating of neutral atom detector parameters
24	589.64	Detection of surrounding solar wind particles with neutral atom detector
25	600.55	Six times of infrared spectrum detection and neutral atom detection

antisymmetrical slip versus skid mechanics (*14*). For a wheel with skidding, the resistance force is in the same direction as the tractive force, both of which are resistance forces that increase with skid ratio. However, the resistance force counteracts the tractive force to decrease the drawbar pull when a wheel slips. As a result, even if the rover moves downward and upward along the same slope, its wheels

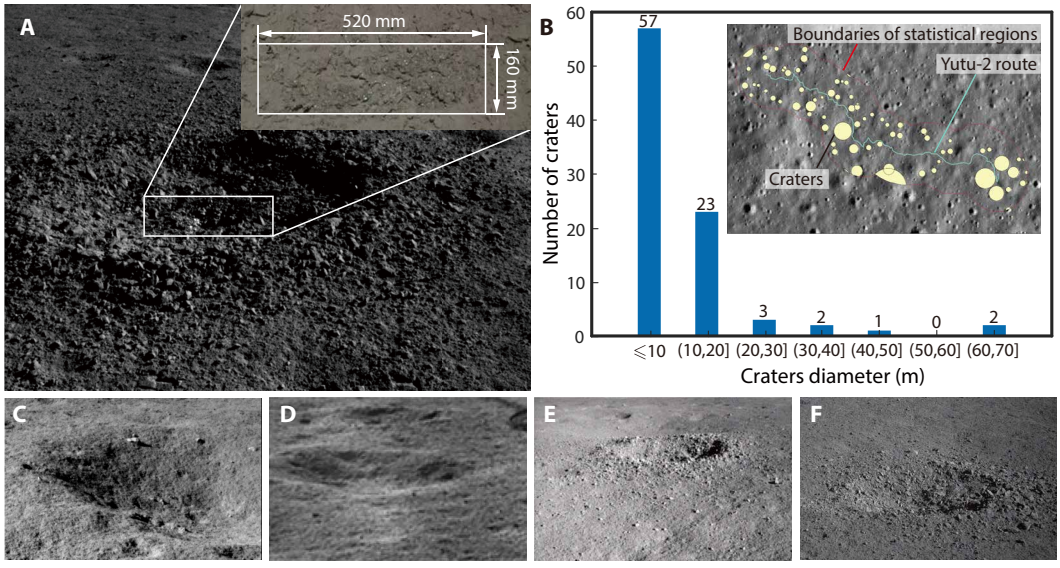

Fig. 5. Craters encountered by Yutu-2 along the traversed route. (**A**) High-reflection materials encountered by Yutu-2 on the ninth lunar day. (**B**) The statistical results on the diameter of craters are identified. The number of craters less than 10 m in diameter is the highest. There are 88 craters identified within 50 m of the routing path of Yutu-2 on the first 25 lunar days. The base image is a LROC NAC image, whose resolution is 1 m. The craters are visually identified and manually mapped based on the LROC NAC mosaic using the ArcGIS add-in tool of "CraterTools," which is independent of the map projection and has been widely used in planetary crater mapping (*62*). Three evenly distributed points on the crater rim are digitized to derive the crater diameter with CraterTools. When digitizing the craters, a local tangent plane projection is adopted so that the craters appear circular, making crater mapping convenient and precise. (**C** and **D**) Old craters that have experienced a relatively long period of space weathering. (**E** and **F**) Fresh craters with ejecta on one side or around.

may not be able to obtain enough drawbar pull for climbing back. Climbing attempts with severe wheel slippage is prone to cause large wheel sinkage, or even rover immobilization, similar to what was experienced by Spirit (*36*) and Opportunity (*36*), especially when traversing on soft and deformable terrain. One of the kernels of solving these problems is modeling fundamental principles of movement for the substrate of complex properties (like solidification or fluidization) during wheel-terrain interaction that relied on "robophysics" study (*37*, *38*) with systematic tests. New theories based on simplified model of dynamic granular intrusion (*39*) and strategies of unconventional gaits of the rover (*40*) developed upon robophysics analysis are promising to cope with these dilemmas.

The CE-4 landing site lacked surface boulders, but Yutu-2 encountered several craters (fig. S8) (*32*). On the basis of the analysis of Lunar Reconnaissance Orbiter Camera (LROC) imagery from the Lunar Reconnaissance Orbiter launched in 2009, 88 impact craters can be quantifiably identified within a 50-m range along Yutu-2's routing path of the first 25 lunar days (Fig. 5B), ranging in diameter from 4.68 to 61.83 m (mean value of 11.89 m). Among them, more than 60% are less than 10 m in diameter, with craters of diameter more than 20 m being rare. From more detailed panoramic stereo images, 20 craters within a 10-m distance from the rover can be measured, all with depths shallower than 0.6 m and depth/diameter ratios (d/D) between 0.04 and 0.12, with the mean d/D value being 0.07 (*33*), suggesting that the craters are relatively fresh. Images acquired by the rover's visual systems along the traverse routes indicate broad morphologies of craters that can be mainly divided into three categories: first are heavily degraded craters (Fig. 5, C and D), with gentle slopes and flat edges bordering the ground, indicating that they have experienced a relatively long period of space weathering; in contrast, other craters (Fig. 5, E and F) have varied grain size ejecta (from fine particles to clods), with coarse walls and bottoms. These craters were further classified into two categories according to the different distributions of their ejecta, either evenly distributed or a skewed distribution to one side.

A high spatial density of fresh craters with unilateral ejecta can be observed at the CE-4 landing site (fig. S8). High-resolution observations (fig. S9) show that the craters are almost all oriented to the northwest; thus, they are inferred to be sourced from the same set of impact events. Considering the impact cratering mechanism, the orientation of the ejecta is in line with the horizontal component of the impact force. Considering the fast overturn rate of surface regolith and small crater sizes, these craters are not assumed to be primary craters, but are most likely secondary craters formed by the Zhinyu crater, which is located to the west of the CE-4 landing site (*32*). Similar ejecta in skewed distribution were also observed at the landing site, as seen from a color image of the lander (fig. S10A). During the near-ground landing phase, the landing legs impacted the surface with oblique forces and dug out subsurface materials to form a one-sided deposit of fine-grained particles and relatively large clods on the summit. In contrast, the ejecta around the CE-3's lander legs (fig. S10B) resembles loose particles and are darker in color, compared with the surficial materials, and accompanied by small gravel.

Rocks along the traverse route (Fig. 6) are relatively rare in comparison with those scattered around the CE-3 landing site in meter size (fig. S11). Some rocks are perched on the surface as a result of projectiles and fragments of impact. As a comparison, unlike the densely clustered, various-sized fragments imaged by Pancam at the CE-3 landing site, rocks at the CE-4 landing site were relatively isolated and of a smaller scale (less than 40 mm); some rocks were sparsely clustered, resembling pearls, whereas others were irregular

or angular. In the CE-4 mission, rocks partially buried by regolith were scarcely observed; furthermore, relatively large rocks, such as those shown in fig. S11 (A to C) from the Mare Imbrium CE-3 site, are absent from observations of the first 25 lunar days. For CE-4, a distinct rock more than 200 mm in size measured by VNIS on the third lunar day was referred to as olivine norite from its spectrogram (similar in mineral composition as the regolith) and its fine-to-medium grain size texture, which was probably the result of relatively fast crystallization related to its origination from the impact melt pond, produced via the melting of the lunar lower crust and mantle materials by the SPA basin–forming event (*22*). A medium-sized (about 300 mm in diameter) angular rock isolated from its surroundings was observed in the onboard navigation camera (Navcam) image taken on the 23rd lunar day (Fig. 6H). Yutu-2 attempted to approach the rock by detouring around an extraordinary crater nicknamed "Longtan," but eventually ceased efforts due to the highly rugged and steeply sloped terrain (12°) and the presence of abundant rocks in the detection area.

The subsurface structure at the landing site, primarily consisting of low-loss, highly porous, granular materials, with embedded boulders of various sizes (*41*), was revealed on the basis of a dual-channel LPR data (CH-1, 60 MHz; CH-2, 500 MHz) (*42*) in both the shallow regolith and the deeper geological strata. The shallow regolith can be separated into three distinct layers according to the distribution, quantity, and dimension of inhomogeneities illustrated in the high-frequency LPR measurements (table S3). At least five strata were detected to the depth of 328 m (*43*), for which a uniform basal layer may be present between 38 and 52 m, followed by further basal layers from different lunar geological periods. The buried ejecta is overlain by at least four layers of distinct lava flows that probably occurred during the Imbrium Epoch, with their thicknesses ranging from 12 m to more than 100 m, providing direct evidence of multiple lava-infilling events that occurred within the Von Kármán crater (*43*). To improve the estimation accuracy of the stratum depth, rectification and analysis of the LPR data are expected to be carried out with consideration of the rover's varying attitude. Furthermore, in situ sampling through drilling of great depth and contact measurements to be carried out in the future missions will accelerate the progress of stratigraphy research in the extraterrestrial environment.

DISCUSSION

This work has described the lunar farside in situ exploration with the Yutu-2 rover on a long-duration, multiyear CE-4 mission. During the mission, Yutu-2 experienced mild wheel slips and observed the surface characteristics and subsurface structure of the lunar farside. Studies into the lunar regolith have revealed increased cohesion in the regolith properties, as compared with that in the CE-3 landing site, presumed as a result of higher percentage of agglutinate due to the longer exposure time and greater degree of space weathering. Summarization of Yutu-2's in situ scientific investigations and discoveries with respect to the observed gel-like material, crater, and rock characteristics, as well as shallow subsurface structure, and additional analysis on differentiated fresh crater morphologies and ejecta distributions provide a comprehensive landscape overview of the lunar farside. Our study explicitly revealed the difference in the soil properties between the nearside and farside of the Moon with supportable in situ evidence. The scientific data and discoveries obtained by Yutu-2 provide new resources on multiple aspects for further studies of the lunar farside and complement our understanding of the Moon.

Although the interesting soil cohesion phenomenon is analyzed to be regional with multiday observations, intensive study of the chemical composition and physical properties of the lunar regolith is necessary to be carried out for further analysis. More notable findings are expected to be discovered by taking full advantage of the rover's capability. For instance, trenching experiments can be conducted using one of the rover's wheels to expose the near-subsurface soil and estimate undisturbed terrain parameters more accurately.

On the basis of in-depth understanding of the lunar farside, more powerful locomotion, higher intelligence, and advanced scientific

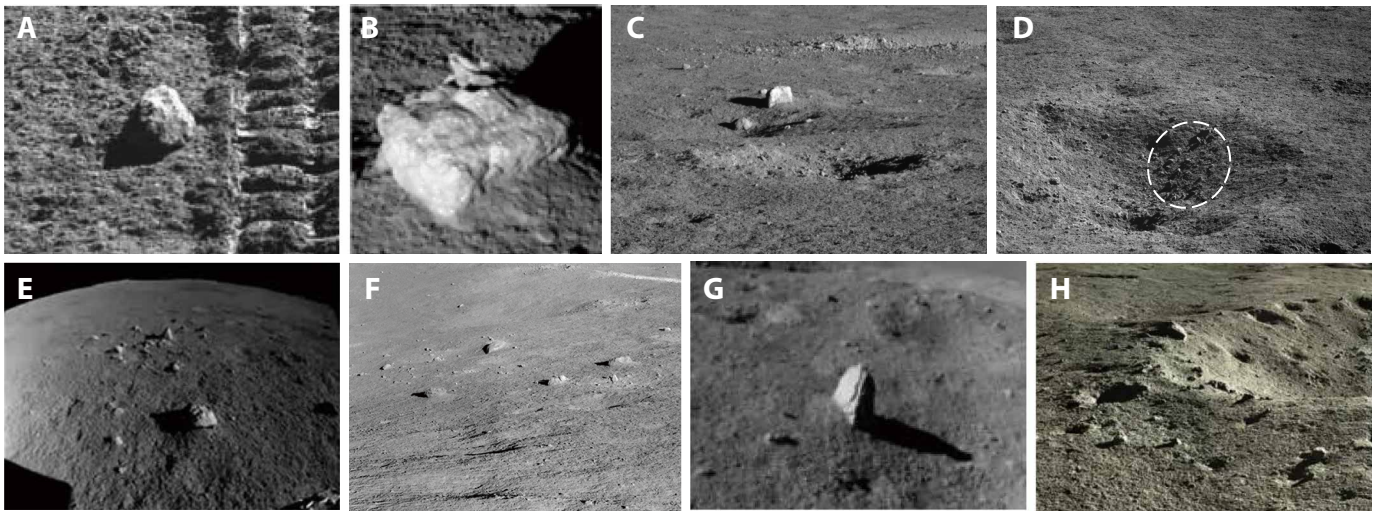

Fig. 6. Rocks encountered by Yutu-2 along the traversed route. (**A**) Isolated rock. (**B**) Rock nicknamed "Qiyuan" discovered on the third lunar day from (*15*). (**C**) Rock perched on the surface. (**D**) Sparsely clustered gravels that are round, like pearls. (**E** and **F**) Sparsely clustered fragments in irregular or angular shapes at CE-4 landing site. (**G**) Unique rock shaped like a sharp fin with a notable bulge in the edge. (**H**) Rock at the rim of crater nicknamed Longtan.

payloads are needed for future lunar exploration with space robots in larger scales and harsher environments. For example, legged robots, hybrid wheel-legged robots, or tethered rovers can be considered for future lunar crater or cave exploration. Physical intelligence (understanding the scenes surpassing purely geometric aspect), through active probing strategies for supportability or stability assessment, is necessary to be developed to cope with the unknown nature of the environment. Besides, targets of interest may be selected and targeted in a more efficient way, as implemented in the Curiosity rover (*44*), and explorations can be carried out in new discovery-oriented autonomous paradigm, with enhanced autonomous situated experimenting abilities. In terms of scientific payloads, diverse payloads for in situ sampling and chemical, physical, and biological analysis may be used with powerful executors and advanced data processing subsystems to break through the content, depth, and efficiency limitations and to satisfy the increasing requirement of comprehensive investigation. In general, multidisciplinary knowledge are expected to be incorporated to make an all-round improvement of rovers for future autonomous exploration to discover new insights into the Moon.

MATERIALS AND METHODS

Instruments and data description

Images used in this study were obtained by three pairs of stereo cameras onboard the rover: Navcam, Pancam, and Hazcam. Navcam and Pancam are mounted on the same camera bar of the rover mast, whereas Hazcam is located at the lower front of the rover body. The Navcam system is composed of two identical cameras, and each camera has the ability to take gray-scale images with a field of view (FOV) of 46.6°. Navcam has a stereo base of 270 mm, with a focal length of 17.7 mm, and the effective image size is 1024 pixels by 1024 pixels (*45*). Each camera of the Pancam has the ability to take color (red: 640 nm, green: 540 nm, blue: 470 nm) and panchromatic (420 to 700 nm) images, with an FOV of 19.6° by 14.5° (*45*). The Pancam's stereo base is 270 mm, and the stereo images can be used to generate high-resolution topographic maps of the lunar surface using photogrammetric techniques. The effective image size is 2352 pixels by 1728 pixels in color mode and 1176 pixels by 864 pixels in panchromatic mode. The Pancam can acquire a 360° panoramic view by taking 56 pairs of images (28 different azimuth angles at two elevation angles) (*45*). In this study, we have used the images acquired by Hazcam to infer the property of the lunar regolith at the CE-4 landing site. Each camera of Hazcam has a fisheye lens that offers a 170° FOV. The Hazcam acquires 1024 pixel–by–1024 pixel stereo images, which are used to obtain 3D terrain information in front of the rover to enable hazard detection (e.g., large rocks and craters) along the rover's pathways (*28*).

Wheels of Yutu-2 are used as a device to characterize the slippage experienced by the rover and identify soil parameters, based on the wheel-terrain interaction. The meshed wheel of Yutu-2 is accompanied by lugs, and each wheel weighs 0.735 kg. Considering the gravity on the Moon, the vertical load on each wheel is estimated, based on the rover configuration and mass distribution at 36.5 N under a quasi-static state. The distance between the left and right wheels is 800 mm. The radius of the wheel is 150 mm, and the width of the wheel is 150 mm. Each wheel is equipped with 24 lugs arranged in two staggered rows. The lugs in each row are evenly arranged on the wheel's outer cylinder surface, at a height of 10 mm.

Cross-site visual localization of Yutu-2

The precise localization of the Yutu-2 rover (hereafter referred to as Yutu-2) was achieved using cross-site visual localization, based on the rover's Navcam images acquired at adjacent sites (waypoints) (*45*). In general, localization of rovers is achieved using the following key steps (*46*): (i) projection: cross-site images are projected to the ground plane to reduce distortions, if captured in opposite directions; (ii) area determination: initial localization results obtained by dead-reckoning are used to calculate the corresponding image area of the adjacent site (considered as the initial matching region) to limit the search range and ensure reliability of the subsequent matching; (iii) matching: images are enhanced for texture and gray-scale consistency, and corresponding points are detected by the affine-scale invariant feature transform (ASIFT) matching algorithm (*47*) in the initial matching regions, and outlier detection is performed to obtain valid matching results; (iv) solving: accurate localization results are finally generated from the exterior orientation parameters derived from the bundle adjustment solution (*48*). Cross-site visual localization was conducted at the teleoperation center in near real time to provide localization results consisting of positions and attitudes in the landing site local (LSL) reference system. The LSL reference system is a north-east-down (NED) right-handed coordinate system, with the origin at the first waypoint; its z axis points down in the local normal direction, x axis points to the north pole, and y axis is orthogonal to the x and z axes. After a simple transformation, the coordinates of Yutu-2's waypoints are provided in the landing site cartographic (LSC) coordinate system, which is an east-north-up (ENU) right-handed local system having the same origin as the LSL reference system, but its z axis points in the local normal direction, y axis points to the north pole, and x axis is orthogonal to the y and z axes (*49*). Previous research (*50*) has reported that the cross-site visual localization yields an accuracy of 4%, which is better than the nominal localization accuracy of 15% obtained from dead reckoning based on inertial measurement unit (IMU) and wheel odometer data. In practice, within a traverse distance of up to 10 m between neighboring waypoints, the localization results of the cross-site visual localization and the dead reckoning from IMU and wheel odometry were generally consistent with differences in the levels of centimeters to decimeters, depending on the severity of rover slippage (*51*).

Average slip ratio estimation between two adjacent waypoints

The slip ratio s of a lugged wheel at each moment t is defined as follows:

$$s(t)=\begin{cases}1-v(t)/(r_s(t)\,\omega(t)) & (r_s(t)\,\omega(t)\ \geq\ v(t), 0\ \leq\ s(t)\ \leq\ 1)\\ r_s(t)\,\omega(t)/v(t)-1 & (r_s(t)\,\omega(t)\ <\ v(t), -1\ \leq\ s(t)\ <\ 0)\end{cases} \quad (1)$$

where $\omega(t)$ is the angular velocity function, $r_s(t)$ is the shearing radius function, and $v(t)$ is the linear velocity function. When the value of s is larger than zero, it indicates that the wheel is slipping; when s is equal to 0, the wheel rolls without slipping or skidding; when s is less than 0, it indicates that the wheel is skidding, with $|s|$ being the values of the skid ratio. In general, a driving wheel slips when moving on a flat terrain or climbing up a slope, whereas it skids when moving down a slope (*13*).

The average slip ratio $\bar{s}$ of a lugged wheel on Yutu-2 over a traverse between two adjacent waypoints can be expressed using the

average angular velocity $\overline{\omega}$, average linear velocity $\overline{v}$, and average shearing radius $\bar{r}_s$ as follows:

$$\overline{\omega} = \int_0^{\Delta t_p} \omega(\tau)\, d\tau / \Delta t_p \tag{2A}$$

$$\overline{v} = \int_0^{\Delta t_p} v(\tau)\, d\tau / \Delta t_p \tag{2B}$$

$$\bar{s} = \begin{cases} 1 - \overline{v}/(\bar{r}_s\overline{\omega}) \; (\bar{r}_s\overline{\omega} \geq \overline{v}, 0 \leq s \leq 1) \\ \bar{r}_s\overline{\omega}/\overline{v} - 1 \; (\bar{r}_s\overline{\omega} < \overline{v}, -1 \leq s < 0) \end{cases} \tag{2C}$$

where Δt_p is the travel time of Yutu-2 between two adjacent waypoints. The average shearing radius, $\bar{r}_s$, can be computed as follows (*13*):

$$\bar{r}_s = r + \lambda_s h \tag{3}$$

where r is the wheel radius, h is the height of the lugs, and λ_s ($1 \leq \lambda_s \leq 0$) is the lug coefficient determined by the number of lugs and the internal friction angle of the soil.

Equation 2C can be rearranged as follows:

$$\bar{s} = \begin{cases} 1 - \overline{v}\Delta t_p/(\bar{r}_s\overline{\omega}\Delta t_p) \; (\bar{r}_s\overline{\omega}\Delta t_p \geq \overline{v}\Delta t_p, 0 \leq s \leq 1) \\ \bar{r}_s\overline{\omega}\Delta t_p/(\overline{v}\Delta t_p) - 1 \; (\bar{r}_s\overline{\omega}\Delta t_p < \overline{v}\Delta t_p, -1 \leq s < 0) \end{cases} \tag{4}$$

and further simplified as

$$\bar{s} = \begin{cases} 1 - L_{gt}/L_p \; (L_p \geq L_{gt}, 0 \leq s \leq 1) \\ L_p/L_{gt} - 1 \; (L_p < L_{gt}, -1 \leq s < 0) \end{cases} \tag{5}$$

where L_p is the planned travel mileage of Yutu-2 derived from locomotion commands and L_{gt} is the actual travel mileage.

Note that Yutu-2 takes images only at waypoints, and no images are captured during the traverse; hence, only the actual travel distance between two waypoints can be obtained. Thus, when Yutu-2 travels in curves, the traverse mileage (arc length) is replaced with its corresponding chord length, which is the travel distance. Considering the locomotion states obtained during a traverse between two adjacent waypoints, Eq. 5 can be further rearranged as follows:

$$\bar{s} = \begin{cases} 1 - D_{gt}/D_p \; (D_p \geq D_{gt}, 0 \leq s \leq 1) \\ D_p/D_{gt} - 1 \; (D_p < D_{gt}, -1 \leq s < 0) \end{cases} \tag{6}$$

where D_p is the planned travel distance of Yutu-2 calculated using the coordinates of the starting and ending waypoints represented by x and y, respectively, and D_{gt} is the actual travel distance of Yutu-2 estimated by visual localization.

In general, accurate wheel slip ratio at each moment can be estimated using Eq. 1 with the measured rover speed. Unfortunately, the speed of Yutu-2 during movement was not available, and Eq. 6 was used for average slip ratio estimation over two adjacent waypoints using the available distance data. In practice, on the basis of the raw localization results of Yutu-2 coordinates in the LSC reference system, the relative position between two adjacent waypoints can be computed as (Δx, Δy), and the actual travel distance can be calculated as $\sqrt{\Delta x^2 + \Delta y^2}$. On the other hand, in the CE-4 mission, the planned waypoints of Yutu-2 are known and given in (x, y) coordinates in the LSC reference system. Thus, it is simple to calculate the planned distance between two adjacent waypoints according to their relative position in the x and y directions, according to the actual travel distance. Although the results calculated using Eq. 6 were obtained without knowing the vehicle speed, they are meaningful because the distance between two waypoints is short (less than 14.28 m) and the terrain slope variation is small. Because, under these conditions, the fluctuation of the wheel slip ratio should not be large, implying that the fluctuation of rovers' velocity is small, together with the equal and constant angular velocities of all the wheels, the effect of speed variation of the vehicle during the movement should be small.

Slip ratio estimation based on wheel trace imprint

Rover trace contours can be used to infer the wheel-terrain interaction characteristics. A clear and intact wheel imprint with a longitudinal slip, as shown in fig. S3, consists of a series of trace units, and each trace unit can be divided into two areas: the lug-sheared area dug out by the lug itself and the hub-pressed area compressed by the wheel hub. The distance between two adjacent trace units is called the trace unit width and is denoted as Δx_p.

The lug-sheared and hub-pressed areas occur alternatively, resulting in a staggered pattern of the trace imprint. A larger slip ratio of the wheel is accompanied by a more compact pattern of lug imprint, and the lug imprint of the trace is condensed with an increase in the wheel slip ratio. Thus, the slip ratio can be estimated based on the structural features of the wheel trace imprints without considering the lateral slip ratio, as follows (*52*):

$$\bar{s} = 1 - \Delta x_p n/(2\pi\bar{r}_s) \; (0 \leq \bar{s} \leq 1) \tag{7}$$

where n is the number of lugs on the wheel. Because n and $\bar{r}_s$ are constants determined by the wheel configuration, $\bar{s}$ can be estimated by measuring Δx_p.

By taking advantage of the same ratio of the trace unit width relative to the wheel width on both the orthograph and the actual size, we can estimate the distance between two adjacent trace units, Δx_p, for a measured length of the trace unit on the trace imprint orthograph, p_u, relative to the length of the wheel width on the trace imprint orthograph p_w:

$$\Delta x_p = b \times \frac{p_u}{p_w} \tag{8}$$

where b is the wheel width.

An image processing method was introduced to extract Δx_p with two key steps: view correction and trace feature extraction. The original image was first corrected with the camera extrinsic matrix to a top-view image. Then, each trace imprint unit was manually divided into independent areas, and trace imprint information, such as the trace unit width, were acquired. The wheel slip ratio was then estimated from the trace imprint using Eq. 7. When a series of continuous trace units were almost of the same width, their average trace unit widths were calculated to reduce the measurement error, and the average wheel slip ratio was deduced to represent the wheel slippage experienced by Yutu-2.

Soil parameter identification

Because Yutu-2 does not carry specific soil parameter identification instruments, the rover wheel was used as a trenching device to

identify soil parameters, based on the wheel-terrain interaction. To estimate the soil parameters, the wheel-terrain interaction should be modeled. For a lugged rover wheel moving on the soft and deformable terrain with an angular velocity ω, as shown in Fig. 4A, the wheel is applied with a vertical load W and a resistance force f_{DP} from the vehicle suspension, as well as a driving torque T at the wheel rotation axis by an actuator. The terrain interacts with the wheel circumference in the contact region, which corresponds to the angle divided into two parts: the entrance angle θ_1 from the vertical, at which the wheel begins to make contact with the soil, and the exit angle θ_2 from the vertical, where the wheel loses contact with the soil. In the wheel-terrain interaction region ($\theta_1 + \theta_2$), the continuous normal stress σ to support the wheel, and the shearing stress τ due to the relative movement are exerted on the wheel surface, as shown in Fig. 4A. The point of maximum stress is denoted as θ_m, according to which the stress region is divided into a forward part (σ_1, τ_1), corresponding to the angle from θ_1 to θ_m, and a rear part (σ_2, τ_2), corresponding to the angle from θ_m to θ_2.

Considering the shape of the wheel surface, the distributed normal stress along the wheel circumference is deduced from the Wong-Reece model (*53*) and improved by considering the slip sinkage and lug effects. The improved model is named Ding's model (*54*), which uses $n_0 + n_1 s$ to substitute for the conventional sinkage exponent n and can be used for small wheels with high slip sinkage. Ding's model can be expressed as follows:

$$\begin{cases} \sigma_1(\theta) = \left(\dfrac{k_c}{b} + k_\varphi\right) r^N (\cos\theta - \cos\theta_1)^N \quad (\theta_m \le \theta \le \theta_1) \\ \sigma_2(\theta) = \left(\dfrac{k_c}{b} + k_\varphi\right) r^N \left\{\cos\left[\theta_1 - \dfrac{\theta - \theta_2}{\theta_m - \theta_2}(\theta_1 - \theta_m)\right] - \cos\theta_1\right\}^N \quad (\theta_2 \le \theta < \theta_m) \end{cases} \tag{9}$$

where b is the width of the wheel, k_c is the cohesive modulus of the soil, k_φ is the frictional modulus of the soil, and N is the variable sinkage exponent of wheel-terrain interaction that can be represented by a linear function of slip ratio s, as follows:

$$N = n_0 + n_1 s \tag{10}$$

where n_0 represents the static sinkage exponent and n_1 represents the dynamic sinkage resulting from wheel slippage. The values of n_0 and n_1 were determined on the basis of experiments, and the introduction of the linear soil sinkage exponent led to a high affinity for fitting the slip-sinkage phenomenon of lugged wheels (*20*). Previously, the dynamic sinkage caused by slip ratio was not considered; thus, it was deemed that $N = n$, where n is the intrinsic sinkage exponent of the terrain.

The entrance angle θ_1 is a function of wheel sinkage z and can be expressed as

$$\theta_1 = \arccos[(r - z)/r] \tag{11}$$

and the exit angle θ_2 can be computed as

$$\theta_2 = c_3 \theta_1 \tag{12}$$

where c_3 is the coefficient of the exit angle, characterizing the ratio of the exit angle θ_2 to the entrance angle θ_1. According to Rankine's theory of earth pressure (*55*), the active earth pressure (caused by the soil rebound) on deformable terrain (stress integration from θ_m to θ_2) is much smaller than the passive pressure (stress integration from θ_1 to θ_m). Therefore, the active earth pressure is generally negligible (*56*), and the corresponding exit angle θ_2 is assumed to be 0. Consequently, the coefficient c_3 for calculating the exit angle θ_2 is taken as zero in the calculation.

The maximum stress angle θ_m can be computed as

$$\theta_m = (c_1 + c_2 s)\theta_1 \tag{13}$$

where c_1 and c_2 are the coefficients of the wheel-terrain interaction angle. In the calculation, c_1 and c_2 are set to 0.5 and 0, respectively, and the value of θ_m is equal to 0.5 times of θ_1. As shown in Fig. 4A, the stress distribution curves (blue line: the normal distribution curve; red line: the shear stress distribution curve) are asymmetric with respect to the angular location of the maximum stress θ_m. However, in this case, θ_2 is assumed to be 0; thus, the angular location of maximum stress θ_m happens to occur midway between θ_1 and θ_2.

The tangential stress $\tau(\theta)$ can be computed as

$$\tau(\theta) = (c + \sigma(\theta)\tan\varphi) \times \{1 - \exp(-r_s[(\theta_1' - \theta) - (1 - s)(\sin\theta_1' - \sin\theta)]/K)\} \tag{14}$$

where c is the cohesion of the soil, φ is the internal friction angle, K is the shearing deformation modulus, r_s is the equivalent shearing radius, and θ_1' is the equivalent entrance angle. With the lug effect, the shearing stress occurs on the surface of the soil sticking to the wheel circumference due to the wheel lugs instead of the wheel outer cylinder surface, and the equivalent shearing radius r_s can therefore be defined as follows (*13*):

$$r_s = r + \lambda_s h \quad (0 \le \lambda_s \le 1) \tag{15}$$

where h and λ_s have aforementioned in Eq. 3. For Yutu-2's wheels, which are evenly equipped with lugs at 10-mm height, the value of λ_s is about 0.5, according to the experimental results in (*13*). The equivalent entrance angle θ_1' of a lugged wheel (*20*) can be computed as follows:

$$\theta_1' = \arccos[(r - z)/(r + h)] \tag{16}$$

When θ approaches θ_m, the corresponding normal stress and tangential stress approach their maximum, expressed as follows:

$$\sigma_m = \left(\frac{k_c}{b} + k_\varphi\right) r^N (\cos\theta_m - \cos\theta_1)^N \tag{17}$$

$$\tau_m = (c + \sigma_m \tan\varphi) \times \{1 - \exp(-r_s[(\theta_1' - \theta_m) - (1 - s)(\sin\theta_1' - \sin\theta_m)]/K)\} \tag{18}$$

When the wheel is in a quasi-static state, the effect of the distributed stress (normal stress σ and tangential stress τ) can be simplified to the normal force F_N, drawbar pull F_{DP}, and driving resistance torque M_R by integrating along the wheel-terrain interaction area, which are balanced with the wheel load W, resistance force f_{DP}, and driving torque T, respectively. For wheels on Yutu-2 having a maximum speed of 200 m/hour, the quasi-static condition is valid because the dynamic effects are negligible at low speeds. Therefore,

the force/torque balance equations for Yutu-2's lugged wheels can be expressed as follows:

$$F_N = b\left\{\int_{\theta_2}^{\theta_m}[r\sigma_2(\theta)\cos\theta + r_s\tau_2(\theta)\sin\theta]d\theta + \int_{\theta_m}^{\theta_1}[r\sigma_1(\theta)\cos\theta + r_s\tau_1(\theta)\sin\theta]d\theta\right\} = W \tag{19A}$$

$$F_{DP} = b\left\{\int_{\theta_2}^{\theta_m}[r_s\tau_2(\theta)\cos\theta - r\sigma_2(\theta)\sin\theta]d\theta + \int_{\theta_m}^{\theta_1}[r_s\tau_1(\theta)\cos\theta - r\sigma_1(\theta)\sin\theta]d\theta\right\} = f_{DP} \tag{19B}$$

$$M_R = r_s^2 b\left[\int_{\theta_2}^{\theta_m}\tau_2(\theta)\,d\theta + \int_{\theta_m}^{\theta_1}\tau_1(\theta)\,d\theta\right] = T \tag{19C}$$

According to Shibly *et al.* (*57*), the wheel-terrain interaction stress can be linearized as follows:

$$\begin{cases}\sigma_1(\theta) = \sigma_m(\theta_1 - \theta)/(\theta_1 - \theta_m)\ (\theta_m \le \theta \le \theta_1)\\ \sigma_2(\theta) = \sigma_m(\theta - \theta_2)/(\theta_m - \theta_2)\ (\theta_2 \le \theta < \theta_m)\end{cases} \tag{20}$$

$$\begin{cases}\tau_1(\theta) = \tau_m(\theta_1 - \theta)/(\theta_1 - \theta_m)\ (\theta_m \le \theta \le \theta_1)\\ \tau_2(\theta) = \tau_m(\theta - \theta_2)/(\theta_m - \theta_2)\ (\theta_2 \le \theta < \theta_m)\end{cases}. \tag{21}$$

Because the entrance angle is usually not large, and when θ approaches θ_1, the corresponding normal stress and tangential stress all approach zero; Ding (*58*) proposed that the product of cosθ and stress can also be linearized, as shown in Eqs. 22 and 23. Let $\sigma'_m = \sigma_m\cos\theta_m$ and $\tau'_m = \tau_m\cos\theta_m$.

$$\begin{cases}\sigma_1(\theta)\cos\theta = \sigma'_m(\theta_1 - \theta)/(\theta_1 - \theta_m)\\ \sigma_2(\theta)\cos\theta = \sigma'_m(\theta - \theta_2)/(\theta_m - \theta_2)\end{cases} \tag{22}$$

$$\begin{cases}\tau_1(\theta)\cos\theta = \tau'_m(\theta_1 - \theta)/(\theta_1 - \theta_m)\\ \tau_2(\theta)\cos\theta = \tau'_m(\theta - \theta_2)/(\theta_m - \theta_2)\end{cases}. \tag{23}$$

By applying Eqs. 20 to 23 in the wheel-terrain interaction model of Eq. 19 and ignoring the vertical component of the shearing stress, we obtained a simplified expression of F_N as follows

$$F_N \approx rb(\theta_1 - \theta_2)\sigma_m\cos\theta_m/2 \tag{24}$$

whereas Eq. 24 can be rearranged as

$$\sigma_m = \frac{2F_N}{rb(\theta_1 - \theta_2)\cos\theta_m} \tag{25}$$

Note that Eqs. 17 and 25 represent two expressions for the maximum normal stress σ_m. σ_m can be calculated using Eq. 25 using the estimated F_N, wheel sinkage, and wheel configuration parameters. The three bearing characteristic parameters, namely, cohesive modulus of soil k_c, frictional modulus of soil k_φ, and sinkage exponent N, remained unknown in Eq. 17. Because Yutu-2's wheels rolled in different contact states with the soil, various σ_m, θ_m, and θ_1 were obtained, which were then used with Eq. 17 to solve the unknown characteristic parameters in that equation. Because the wheel width b for Yutu-2 is a constant and the bearing characteristic parameters k_c, k_φ, and N for the same type of soil are also constants, the term $(k_c/b + k_\varphi)$ in Eq. 17 is a constant. Thus, under these conditions, k_c and k_φ cannot be solved using Eq. 17.

Therefore, the equivalent stiffness modulus K_s ($K_s = k_c/b + k_\varphi$) was estimated, instead of k_c and k_φ. The typical values of N obtained from the Apollo 15 mission were used with Eq. 17 to obtain the estimated soil stiffness K_s, which indicates the comparative stiffness of the lunar soil on the farside compared with that estimated for the soil sample obtained from the Apollo missions. The same method was used to estimate N of the soil. The process is illustrated in fig. S12.

In practice, the values of wheel radius r, wheel width b, wheel lug height h, and equivalent radius r_s were constant and determined by Yutu-2's wheel configuration, as shown in table S1. The normal force F_N was estimated from the vertical load W, which can be computed from a quasi-static force analysis of the rover with the knowledge of rover configuration and mass distribution. The two key wheel motion state variables, slip ratio s and sinkage z, can be computed using vision-based techniques or by kinematic analysis of the rover suspension. The wheel sinkage in this study was estimated on the basis of images (fig. S6) that show the edges of the rover wheels. Through image processing (*59*), the circular contour of the wheel and the crooked wheel-interaction curve were extracted on the orthographic image of the rover wheel. Then, the curve was fitted into a straight line using the least squares method on the pixel plane, as shown in fig. S13. Furthermore, the radius of the wheel r_p and the distance of the wheel center to the wheel-terrain interaction line l_p on the pixel plane were acquired, and the wheel sinkage was then estimated using the following equation:

$$z = \frac{r_p - l_p}{r_p}r_m \tag{26}$$

where z is the wheel sinkage and r_m is the actual radius of the wheel. The soil-bearing characteristic parameters of the Apollo mission from (*21*)—including the cohesive modulus k_c, frictional modulus k_φ, and sinkage exponent N—are also shown in table S1. On the basis of the given parameters, for a wheel sinkage of 10 mm, the equivalent stiffness modulus (denoted by K_s) was estimated to be 1280 kPa/m^N, and the sinkage exponent N was estimated to be 0.91.

SUPPLEMENTARY MATERIALS

www.science.org/doi/10.1126/scirobotics.abj6660
Figs. S1 to S13
Tables S1 to S3
Data files S1 to S4

REFERENCES AND NOTES

1. C. M. Pieters, J. N. Goswami, R. N. Clark, M. Annadurai, J. Boardman, B. Buratti, J.-P. Combe, M. D. Dyar, R. Green, J. W. Head, C. Hibbitts, M. Hicks, P. Isaacson, R. Klima, G. Kramer, S. Kumar, E. Livo, S. Lundeen, E. Malaret, T. McCord, J. Mustard, J. Nettles, N. Petro, C. Runyon, M. Staid, J. Sunshine, L. A. Taylor, S. Tompkins, P. Varanasi, Character and spatial distribution of OH/H_2O on the surface of the Moon seen by M3 on Chandrayaan-1. *Science* **326**, 568–572 (2009).
2. C. Zeitlin, D. M. Hassler, F. A. Cucinotta, B. Ehresmann, R. F. Winner-Schweingruber, D. E. Brinza, S. Kang, G. Weigle, S. Bottcher, E. Bohm, S. Burmeister, J. Guo, J. Kohler, C. Martin, A. Posner, S. Rafkin, G. Reitz, Measurements of energetic particle radiation in transit to Mars on the Mars Science Laboratory. *Science* **340**, 1080–1084 (2013).
3. L. Xiao, P. Zhu, G. Fang, Z. Xiao, Y. Zou, J. Zhao, N. Zhao, Y. Yuan, L. Qiao, X. Zhang, H. Zhang, J. Wang, J. Huang, Q. Huang, Q. He, B. Zhou, Y. Ji, Q. Zhang, S. Shen, Y. Li, Y. Gao, A young multilayered terrane of the northern Mare Imbrium revealed by Chang'e-3 mission. *Science* **347**, 1226–1229 (2015).
4. M. Anand, I. A. Crawford, M. Balat-Pichelin, S. Abanades, W. van Westrenen, G. Péraudeau, R. Jaumann, W. Seboldt, A brief review of chemical and mineralogical resources on the Moon and likely initial in situ resource utilization (ISRU) applications. *Planet. Space Sci.* **74**, 42–48 (2012).

5. N. Namiki, T. Iwata, K. Matsumoto, H. Hanada, H. Noda, S. Goossens, M. Ogawa, N. Kawano, K. Asari, S. Tsuruta, Y. Ishihara, Q. Liu, F. Kikuchi, T. Ishikawa, S. Sasaki, C. Aoshima, K. Kurosawa, S. Sugita, T. Takano, Farside gravity field of the Moon from four-way doppler measurements of SELENE (Kaguya). *Science* **323**, 900–905 (2009).
6. D. J. Lawrence, W. C. Feldman, B. L. Barraclough, A. B. Binder, R. C. Elphic, S. Maurice, D. R. Thomsen, Global elemental maps of the Moon: The lunar prospector gamma-ray spectrometer. *Science* **281**, 1484–1489 (1998).
7. J. Liu, X. Ren, W. Yan, C. Li, H. Zhang, Y. Jia, X. Zeng, W. Chen, X. Gao, D. Liu, X. Tan, X. Zhang, T. Ni, H. Zhang, W. Zuo, Y. Su, W. Wen, Descent trajectory reconstruction and landing site positioning of Chang'e-4 on the lunar farside. *Nat. Commun.* **10**, 4229 (2019).
8. P. Norris, *Returning People to the Moon After Apollo: Will It Be Another Fifty Years* (Springer, 2019).
9. G. Fang, B. Zhou, Y. Ji, Q. Zhang, S. Shen, Y. Li, H. Guan, C. Tang, Y. Gao, W. Lu, S. Ye, H. Han, J. Zheng, S. Wang, Lunar Penetrating Radar onboard the Chang'e-3 mission. *Res. Astron. Astrophys.* **14**, 1607–1622 (2014).
10. M. Wieser, S. Barabash, X.-D. Wang, A. Grigoriev, A. Zhang, C. Wang, W. Wang, The advanced small analyzer for neutrals (ASAN) on the Chang'e-4 rover Yutu-2. *Space Sci. Rev.* **216**, 73 (2020).
11. L. Zhang, L. Xiong, J. Sun, L. Chen, One year on-orbit operation of Queqiao lunar relay communications satellite. *J. Aerosp. China* **20**, 5–13 (2019).
12. Y. Wang, W. Wan, S. Gou, M. Peng, Z. Liu, K. Di, L. Li, T. Yu, J. Wang, X. Cheng, Vision-based decision support for rover path planning in the Chang'e-4 mission. *Remote Sens.* **12**, 624 (2020).
13. L. Ding, H. Gao, Z. Deng, K. Yoshida, Slip ratio for lugged wheeled of planetary rover in deformable soil: Definition and estimation, in *Proceedings of the 2009 IEEE/RSJ International Conference on Intelligent Robots and Systems* (IEEE, 2009), pp. 3343–3348.
14. L. Ding, H. Gao, Z. Deng, J. Guo, G. Liu, Longitudinal slip versus skid of planetary rovers' wheels traversing on deformable slopes, in *Proceedings of the 2013 IEEE/RSJ International Conference on Intelligent Robots and Systems* (IEEE, 2013), pp. 2842–2848.
15. S. Gou, Z. Yue, K. Di, W. Wan, Z. Liu, B. Liu, M. Peng, Y. Wang, Z. He, R. Xu, In situ spectral measurements of space weathering by Chang'e-4 rover. *Earth Planet. Sci. Lett.* **535**, 116117 (2020).
16. Z. Wang, Y. Wu, D. T. Blewett, E. A. Cloutis, Y. Zheng, J. Chen, Submicroscopic metallic iron in lunar soils estimated from the in situ spectra of the Chang'e-3 mission. *Geophys. Res. Lett.* **44**, 3485–3492 (2017).
17. Z. Tang, J. Liu, X. Wang, X. Ren, W. Chen, W. Yan, X. Zhang, X. Tan, X. Zeng, D. Liu, H. Zhang, W. Wen, W. Zuo, Y. Su, J. Yang, C. Li, Physical and mechanical characteristics of lunar soil at the Chang'e-4 landing site. *Geophys. Res. Lett.* **47**, e2020GL089499 (2020).
18. J. Y. Wong, *Theory of Ground Vehicles* (John Wiley & Sons, 2008).
19. Y. Gao, C. Spiteri, C.-L. Li, Y.-C. Zheng, Lunar soil strength estimation based on Chang'e-3 images. *Adv. Space Res.* **58**, 1893–1899 (2016).
20. L. Ding, Z. Deng, H. Gao, J. Tao, K. D. Iagnemma, G. Liu, Interaction mechanics model for rigid driving wheels of planetary rovers moving on sandy terrain with consideration of multiple physical effects. *J. Field Robot.* **32**, 827–859 (2015).
21. B. M. French, G. Heiken, D. Vaniman, *Lunar Sourcebook: A User's Guide to the Moon* (Cambridge Univ. Press, 1991).
22. H. Lin, Z. He, W. Yang, Y. Lin, R. Xu, C. Zhang, M. Zhu, R. Chang, J. Zhang, C. Li, H. Lin, Y. Liu, S. Gou, Y. Wei, S. Hu, C. Xue, J. Yang, J. Zhong, X. Fu, W. Wan, Y. Zou, Olivine-norite rock detected by the lunar rover Yutu-2 likely crystallized from the SPA-impact melt pool. *Natl. Sci. Rev.* **7**, 913–920 (2019).
23. S. Gou, K. Di, Z. Yue, Z. Liu, Z. He, R. Xu, H. Lin, B. Liu, M. Peng, W. Wan, Y. Wang, J. Liu, Lunar deep materials observed by Chang'e-4 rover. *Earth Planet. Sci. Lett.* **528**, 115829 (2019).
24. J. Huang, Z. Xiao, L. Xiao, B. Horgan, X. Hu, P. Lucey, X. Xiao, S. Zhao, Y. Qian, H. Zhang, C. Li, R. Xu, Z. He, J. Yang, B. Xue, Q. He, J. Zhong, H. Lin, C. Huang, J. Xie, Diverse rock types detected in the lunar South Pole-Aitken Basin by the Chang'e-4 lunar mission. *Geology* **48**, 723–727 (2020).
25. J. Zhang, B. Zhou, Y. Lin, M. Zhu, H. Song, Z. Dong, Y. Gao, K. Di, W. Yang, H. Lin, J. Yang, E. Liu, L. Wang, Y. Lin, C. Li, Z. Yue, Z. Yao, Z. Ouyang, Lunar regolith and substructure at Chang'e-4 landing site in South Pole–Aitken basin. *Nat. Astron.* **5**, 25–30 (2021).
26. H. Lin, R. Xu, W. Yang, Y. Lin, Y. Wei, S. Hu, Z. He, L. Qiao, W. Wan, In situ photometric experiment of lunar regolith with visible and near-infrared imaging spectrometer on board the Yutu-2 lunar rover. *J. Geophys. Res.-Planets* **125**, e2019JE006076 (2020).
27. J. Lai, Y. Xu, X. Zhang, L. Xiao, Q. Yan, X. Meng, B. Zhou, Z. Dong, D. Zhao, Comparison of dielectric properties and structure of lunar regolith at Chang'e-3 and Chang'e-4 landing sites revealed by ground-penetrating radar. *Geophys. Res. Lett.* **46**, 12783–12793 (2019).
28. S. Gou, Z. Yue, K. Di, J. Wang, W. Wan, Z. Liu, B. Liu, M. Peng, Y. Wang, Z. He, R. Xu, Impact melt breccia and surrounding regolith measured by Chang'e-4 rover. *Earth Planet. Sci. Lett.* **544**, 116378 (2020).
29. Z. Dong, X. Feng, H. Zhou, C. Liu, Z. Zeng, J. Li, W. Liang, Properties analysis of lunar regolith at Chang'E-4 landing site based on 3D velocity spectrum of Lunar Penetrating Radar. *Remote Sens.* **12**, 629 (2020).
30. C. Li, D. Liu, B. Liu, X. Ren, J. Liu, Z. He, W. Zuo, X. Zeng, R. Xu, X. Tan, X. Zhang, W. Chen, R. Shu, W. Wen, Y. Su, H. Zhang, Z. Ouyang, Chang'e-4 initial spectroscopic identification of lunar far-side mantle-derived materials. *Nature* **569**, 378–382 (2019).
31. X.-H. Fu, L. Qiao, J. Zhang, Z.-C. Ling, B. Li, The subsurface structure and stratigraphy of the Chang'E-4 landing site: Orbital evidence from small craters on the Von Kármán crater floor. *Res. Astron. Astrophys.* **20**, 008 (2020).
32. C. Ding, Z. Xiao, B. Wu, Y. Li, N. C. Prieur, Y. Cai, Y. Su, J. Cui, Fragments delivered by secondary craters at the Chang'e-4 landing site. *Geophys. Res. Lett.* **47**, e2020GL087361 (2020).
33. M. Jia, K. Di, Z. Yue, B. Liu, W. Wan, S. Niu, J. Liu, W. Cheng, Y. Ling, Multi-scale morphologic investigation of craters in the Chang'e-4 landing area. *Icarus* **355**, 114164 (2021).
34. Z. Xu, J. Guo, R. F. Wimmer-Schweingruber, J. L. Freiherr von Forstner, Y. Wang, N. Dresing, H. Lohf, S. Zhang, B. Heber, M. Yang, First solar energetic particles measured on the lunar far-side. *Astrophys. J. Lett.* **902**, L30 (2020).
35. Y. Jia, Y. Zou, J. Ping, C. Xue, J. Yan, Y. Ning, The scientific objectives and payloads of Chang'e-4 mission. *Planet. Space Sci.* **162**, 207–215 (2018).
36. R. Gonzalez, K. Iagnemma, Slippage estimation and compensation for planetary exploration rovers: State of the art and future challenges. *J. Field Robot.* **35**, 564–577 (2018).
37. Y. O. Aydin, J. M. Rieser, C. M. Hubicki, W. Savoie, D. I. Goldman, *Robotic Systems and Autonomous Platforms: Advances in Materials and Manufacturing* (Woodhead Publishing, 2019).
38. J. Aguilar, T. Zhang, F. Qian, M. Kingsbury, B. McInroe, N. Mazouchova, C. Li, R. Maladen, C. Gong, M. Travers, R. L. Hatton, H. Choset, P. B. Umbanhowar, D. I. Goldman, A review on locomotion robophysics: The study of movement at the intersection of robotics, soft matter and dynamical systems. *Rep. Prog. Phys.* **79**, 110001 (2016).
39. S. Agarwal, A. Karsai, D. I. Goldman, K. Kamrin, Surprising simplicity in the modeling of dynamic granular intrusion. *Sci. Adv.* **7**, abe0631 (2021).
40. S. Shrivastava, A. Karsai, Y. O. Aydin, R. Pettinger, W. Bluethmann, R. O. Ambrose, D. I. Goldman, Material remodeling and unconventional gaits facilitate locomotion of a robophysical rover over granular terrain. *Sci. Robot.* **5**, aba3499 (2020).
41. C. Li, Y. Su, E. Pettinelli, S. Xing, C. Ding, J. Liu, X. Ren, S. E. Lauro, F. Soldovieri, X. Zeng, X. Gao, W. Chen, S. Dai, D. Liu, G. Zhang, W. Zuo, W. Wen, Z. Zhang, X. Zhang, H. Zhang, The Moon's farside shallow subsurface structure unveiled by Chang'e-4 Lunar Penetrating Radar. *Sci. Adv.* **6**, eaay6898 (2020).
42. L. Zhang, J. Li, Z. Zeng, Y. Xu, C. Liu, S. Chen, Stratigraphy of the Von Kármán crater based on Chang'e-4 Lunar Penetrating Radar data. *Geophys. Res. Lett.* **47**, e2020GL088680 (2020).
43. J. Lai, Y. Xu, R. Bugiolacchi, X. Meng, L. Xiao, M. Xie, B. Liu, K. Di, X. Zhang, B. Zhou, S. Shen, L. Xu, First look by the Yutu-2 rover at the deep subsurface structure at the lunar farside. *Nat. Commun.* **11**, 3426 (2020).
44. R. Francis, T. Estlin, G. Doran, S. Johnstone, D. Gaines, V. Verma, M. Burl, J. Frydenvang, S. Montano, R. C. Wiens, S. Schaffer, O. Gasnault, L. DeFlores, D. Blaney, B. Bornstein, AEGIS autonomous targeting for ChemCam on Mars Science Laboratory: Deployment and results of initial science team use. *Sci. Robot.* **2**, aan4582 (2017).
45. Z. Liu, K. Di, J. Li, J. Xie, X. Cui, L. Xi, W. Wan, M. Peng, B. Liu, Y. Wang, S. Gou, Z. Yue, T. Yu, L. Li, J. Wang, C. Liu, X. Xin, M. Jia, Z. Bo, J. Liu, R. Wang, S. Niu, K. Zhang, Y. You, B. Liu, J. Liu, Landing site topographic mapping and rover localization for Chang'e-4 mission. *Sci. China Inf. Sci.* **63**, 140901 (2020).
46. W. Wan, Z. Liu, K. Di, B. Wang, J. Zhou, A cross-site visual localization method for Yutu rover. *ISPRS J. Photogramm. Remote Sens.* **40**, 279 (2014).
47. J. M. Morel, G. Yu, ASIFT: A new framework for fully affine invariant image comparison. *SIAM J. Imaging Sci.* **2**, 438–469 (2009).
48. B. Triggs, A. Zisserman, R. Szeliski, *Vision Algorithms: Theory and Practice* (Springer, 1999).
49. Z. Liu, K. Di, M. Peng, W. Wan, B. Liu, L. Li, T. Yu, B. Wang, J. Zhou, H. Chen, High precision landing site mapping and rover localization for Chang'e-3 mission. *Sci. China Phys. Mech. Astron.* **58**, 1–11 (2015).
50. W. Wan, thesis, Chinese of Academy of Sciences (2012).
51. J. Wang, J. Li, S. Wang, T. Yu, Z. Rong, X. He, Y. You, Q. Zou, W. Wan, Y. Wang, S. Gou, B. Liu, M. Peng, K. Di, Z. Liu, M. Jia, X. Xin, Y. Chen, X. Cheng, X. Feng, C. Liu, S. Han, X. Liu, Computer vision in the teleoperation of the Yutu-2 rover, in *Proceedings of the Remote Sensing and Spatial Information Science ISPRS Geospatial Week* (International Society for Photogrammetry and Remote Sensing, 2020), pp. 595–602.
52. N. Li, thesis, Harbin Institute of Technology (2019).

53. J. Y. Wong, A. R. Reece, Prediction of rigid wheel performance based on the analysis of soil-wheel stresses part I. Performance of driven rigid wheels. *J. Terramech.* **4**, 81–98 (1967).
54. L. Ding, H. Gao, Z. Liu, Z. Deng, G. Liu, Identifying mechanical property parameters of planetary soil using in-situ data obtained from exploration rovers. *Planet. Space Sci.* **119**, 121–136 (2015).
55. W. J. M. Rankine II, On the stability of loose earth. *Philos. Trans. R. Soc. Lond.* **147**, 9–27 (1857).
56. K. Terzaghi, R. B. Peck, G. Mesri, *Soil Mechanics in Engineering Practice* (John Wiley & Sons, 1996).
57. H. Shibly, K. Iagnemma, S. Dubowsky, An equivalent soil mechanics formulation for rigid wheels in deformable terrain, with application to planetary exploration rovers. *J. Terramech.* **42**, 1–13 (2005).
58. L. Ding, thesis, Harbin Institute of Technology (2009).
59. H. Gao, F. Lv, B. Yuan, N. Li, L. Ding, N. Li, G. Liu, Z. Deng, Sinkage definition and visual detection for planetary rovers wheels on rough terrain based on wheel-soil interaction boundary. *Robot. Auton. Syst.* **98**, 222–240 (2017).
60. B. Liu, S. Niu, X. Xin, M. Jia, K. Di, Z. Liu, M. Peng, Z. Yue, High precision DTM and DOM generation using multi-source orbital data on Chang'E-4 landing site, in *Proceedings of the International Archives of the Photogrammetry, Remote Sensing and Spatial Information Sciences* (International Society for Photogrammetry and Remote Sensing, 2019), pp. 1413–1417.
61. M. S. Robinson, S. M. Brylow, M. Tschimmel, D. Humm, S. J. Lawrence, P. C. Thomas, B. W. Denevi, E. Bowman-Cisneros, J. Zerr, M. A. Ravine, M. A. Caplinger, F. T. Ghaemi, J. A. Schaffner, M. C. Malin, P. Mahanti, A. Bartels, J. Anderson, T. N. Tran, E. M. Eliason, A. S. McEwen, E. Turtle, B. L. Jolliff, H. Hiesinger, Lunar Reconnaissance Orbiter Camera (LROC) instrument overview. *Space Sci. Rev.* **150**, 81–124 (2010).
62. T. Kneissl, S. van Gasselt, G. Neukum, Map-projection-independent crater size-frequency determination in GIS environments—New software tool for ArcGIS. *Planet. Space Sci.* **59**, 1243–1254 (2011).
63. Y. Yang, H. Lin, Y. Liu, Y. Lin, Y. Wei, S. Hu, W. Yang, R. Xu, Z. He, Y. Zou, The effects of viewing geometry on the spectral analysis of lunar regolith as inferred by in situ spectrophotometric measurements of Chang'e-4. *Geophys. Res. Lett.* **47**, e2020GL087080 (2020).

Acknowledgments: We thank all the scientists and engineers who contributed to the Chang'E-4 mission—in particular those from the China Academy of Space Technology (CAST), Shanghai Academy of Spaceflight Technology (SAST), Harbin Institute of Technology (HIT), and Beijing Aerospace Control Center (BACC)—for their dedicated work on the Yutu-2 lunar rover. **Funding:** This work was supported in part by the National Natural Science Foundation of China (grant nos. 51822502, 91948202, and 41771488), in part by the National Key Research and Development Program of China (grant no. 2019YFB1309500), in part by the Fundamental Research Funds for the Central Universities (grant no. FRFCU9803500621), in part by the "111 Project" (grant no. BP0719002), and in part by the Heilongjiang Postdoctoral Fund (grant no. LBH-Z20136). **Author contributions:** L.D. coordinated and wrote the manuscript with R.Z. and Y.Y. T.Y. led the Yutu-2 rover operation and data acquisition. H.G. coordinated coauthor contributions. Data and image analysis: L.D., R.Z., Y.Y., H. Yang, H.G., S. Li, Z. Deng, N.L., Z.W., Z.G., L.H., Z.L., and H. Yu. Rover operations and data acquisitions: J.L., T.Y., C.L., J.W., J.X., S.W., Z.R., D.D., X.W., S.H., K.Z., L.L., X.H., and S. Liu. Rover parameter provision and analysis: Y.J., B.C., and Z. Dang. Crater statistics analysis and geological interpretation: W.W., S.G., and K.D. Results and writing refinement: G.L. and L.R. All authors reviewed and revised the manuscript. **Competing interests:** The authors declare that they have no competing interests. **Data and materials availability:** All data needed to evaluate the conclusions in the paper are present in the paper or the Supplementary Materials. Raw locomotion data of Yutu-2 rover for the first 25 lunar days are provided in data file S1. Working time records of Yutu-2 rover for the first 25 lunar days are provided in data file S2. Elevations along Yutu-2's routing path for the first 25 lunar days are provided in data file S3. Craters within 50 m of Yutu-2's routing path for the first 25 lunar days are provided in data file S4.

Submitted 25 May 2021
Accepted 15 December 2021
Published 19 January 2022
10.1126/scirobotics.abj6660

Science Robotics

A 2-year locomotive exploration and scientific investigation of the lunar farside by the Yutu-2 rover

L. Ding, R. Zhou, Y. Yuan, H. Yang, J. Li, T. Yu, C. Liu, J. Wang, S. Li, H. Gao, Z. Deng, N. Li, Z. Wang, Z. Gong, G. Liu, J. Xie, S. Wang, Z. Rong, D. Deng, X. Wang, S. Han, W. Wan, L. Richter, L. Huang, S. Gou, Z. Liu, H. Yu, Y. Jia, B. Chen, Z. Dang, K. Zhang, L. Li, X. He, S. Liu, and K. Di

Sci. Robot. **7** (62), eabj6660. DOI: 10.1126/scirobotics.abj6660

Science Robotics (ISSN 2470-9476) is published by the American Association for the Advancement of Science. 1200 New York Avenue NW, Washington, DC 20005. The title *Science Robotics* is a registered trademark of AAAS.